Zhao, G., Liu, J., Chen, B., Kaban, M. K., Zheng, X. (2020): Moho Beneath Tibet Based on a Joint Analysis of Gravity and Seismic Data. - Geochemistry Geophysics Geosystems (G3), 21, 2, e2019GC008849.

https://doi.org/10.1029/2019GC008849

Geochemistry, Geophysics, Geosystems

RESEARCH ARTICLE
10.1029/2019GC008849

Moho Beneath Tibet Based on a Joint Analysis of Gravity and Seismic Data

Guangdong Zhao[1,2], Jianxin Liu[1,3], Bo Chen[1,3], Mikhail.K. Kaban[2,4], and Xuanyu Zheng[1]

[1]School of Geosciences and Info-Physics, Central South University, Changsha, China, [2]GFZ German Research Centre for Geosciences, Potsdam, Germany, [3]Hunan Key Laboratory of Non-ferrous Resources and Geological Hazard Detection, Changsha, China, [4]Schmidt Institute of Physics of the Earth, RAS, Moscow, Russia

Key Points:
- The improved Parker's formula guarantees high accuracy
- Gravity effect of the crustal and upper mantle density variations is removed
- New Moho beneath Tibet well corresponds to seismic data

Supporting Information:
- Supporting Information S1
- Figure S1
- Figure S2
- Figure S3
- Figure S4
- Figure S5
- Figure S6
- Figure S7

Correspondence to:
B. Chen,
bochen@csu.edu.cn

Citation:
Zhao, G., Liu, J., Chen, B., Kaban, M. K., & Zheng, X. (2020). Moho Beneath Tibet Based on a Joint Analysis of Gravity and Seismic Data. *Geochemistry, Geophysics, Geosystems*, *21*, e2019GC008849. https://doi.org/10.1029/2019GC008849

Received 2 DEC 2019
Accepted 13 JAN 2020
Accepted article online 15 JAN 2020

Abstract We use the improved Parker-Oldenburg's formulas that include a reference depth into the exponential term and employ the Gauss-fast Fourier transform method to determine Moho depth beneath the Tibetan Plateau. The synthetic models demonstrate that the improved Parker's formula has high accuracy with the maximum absolute error less than 0.25 mGal compared to the analytical solution. Two inversion parameters, that is, the reference depth and the density contrast, are essential for the Moho estimation based on the gravity field, and they need to be determined in advance to obtain correct results. Therefore, the Moho estimates derived from existing seismic studies are used to reduce the nonuniqueness of the gravity inversion and to determine these parameters by searching for the maximum correlation between the gravity-inverted and seismic-derived Moho depths. Another critical issue is to remove beforehand the gravity effects of other factors, which affect the observed gravity field besides Moho variations. In addition to the topography, the gravity effects of the sedimentary layer and crystalline crust are removed based on existing crustal models, while the upper mantle impact is determined based on the seismic tomography model. The inversion results show that the Moho structure under the Tibetan plateau is very complex with the depths varying from about 30–40 km in the surrounding basins (e.g., Ganges basin, Sichuan basin, and Tarim basin) to 60–80 km within the plateau. This considerable difference up to 40 km on the Moho depth reveals the substantial uplift and thickening of the crust in the Tibetan Plateau. Furthermore, two visible "Moho depression belts" are observed within the plateau with the maximum Moho deepening along the Indus-Tsangpo Suture and along the northern margin of Tibet bounding the Tarim basin with the relatively shallow Moho in central Tibet between them. The southern "belt" is likely formed in compressional environment, where the Indian plate underthrusts northward beneath the Tibetan Plateau, while the northern one could be formed by the southward underthrust of the Asian lithosphere beneath Tibet.

1. Introduction

The Tibetan Plateau, known as the roof of the Earth, is the result of the collision and postcollisional convergence of the Indian and Eurasian plates since approximately 50 million years ago (e.g., Dewey et al., 1988; Royden et al., 2008; Yin & Harrison, 2000). It is considered as the "Golden Key" for understanding plate tectonics, continental collisions and continental orogenic formation (Gao et al., 2013; Tapponnier et al., 1982). Knowledge of the Moho topography is essential for many applications, for example, for analysis of elastic deformations of the lithosphere (e.g., Audet & Burgmann, 2011; Chen et al., 2013, 2015), geodynamic modeling (e.g., Hatzfeld & Molnar, 2010). A reliable Moho structure is also vital for understanding the deformation mechanism of the Tibetan Plateau; therefore, these data have been widely used in such studies (e.g., Sun et al., 2012; Zhang et al., 2012; Zhang et al., 2014).

Seismic methods were extensively used to determine the Moho topography beneath the Tibetan Plateau, primarily including seismic reflection (e.g., Gao et al., 2013; Lu et al., 2009; Zhang & Klemperer, 2005; see Zhang et al. (2013), for a review), deep seismic sounding profiles (e.g., Teng et al., 2013, 2014; Wang et al., 2017), receiver function analysis (e.g., Kind et al., 2002; Lou et al., 2009; Singh et al., 2017; Tian et al., 2014; see Li et al. (2014) for a review), and seismic tomography (e.g., Koulakov et al., 2015; Obrebski et al., 2012). Recently, some regional models for the China mainland (Li et al., 2014), Asia and adjacent areas (Stolk et al., 2013), and the global models (e.g., Szwillus et al., 2019) have been compiled by interpolating the

available seismic data to even grids. These seismic surveys could partially provide valuable data on the crustal structure beneath the Tibetan Plateau and reveal that the Moho depth varies from 35–40 km in India to 70–80 km beneath Tibet and up to 85 km in southern Tibet (e.g., Nábělek et al., 2009), approximately double of the global average Moho depth in the continents. However, a large part of this region is still not covered by seismic studies due to the remoteness and extreme climate. Most of these seismic studies only provide Moho estimations beneath single seismic stations or along the profiles, while significant uncertainties may appear by interpolation in the regions with no seismic coverage.

These limitations could be partially mitigated by using the global coverage high-resolution satellite gravity data, particularly in the regions where seismic data are sparse or missed (Chen & Tenzer, 2017). Several studies have been carried out to estimate the Moho depths in the Tibet area using the gravity data (e.g., Bagherbandi, 2012; Braitenberg et al., 2000, 2003; Gómez-Ortiz & Agarwal, 2005; Shin et al., 2007, 2009, 2015; Tenzer, Chen, & Jin, 2015; Xu et al., 2017; Zhang et al., 2015). For example, Braitenberg et al. (2000, 2003) found that the Moho depth under most of Tibet is within 70–75 km, with the maximum Moho depth ~80 km along the margins of the plateau and a shallower depth of ~65 km under the Bangong-Nujiang suture in central Tibet. Tenzer et al. (2013) showed that the Moho depth is largely between 65 and 75 km in Tibet, while the maximum Moho depth reaching to ~79 km is found in the Himalayas and northern Tibet. Shin et al. (2015) found distinct Moho folds in central Tibet, which have been interpreted as the north-south extrusion resulting from the India-Eurasia convergence. Xu et al. (2017) found a remarkable Moho offset of approximately 5 km beneath the Yarlung-Zangbo Suture. Although these researches provided the Moho variations for the whole Tibet area, the estimated Moho depths are noticeably different owing to the different data, modeling tools employed, and the inherent uniqueness of the gravity inversion. Furthermore, the difference between the gravity derived Moho depths and seismic determinations is often very large. The main reason is that the gravity field is affected by all density anomalies in the Earth, while the inversion is usually performed with respect to the Moho variations only. Therefore, determination of the Moho depth beneath Tibet is still controversial and further studies are required.

Several methods were developed to obtain Moho depth by using the gravity data, for example, the isostatic approach solving the Vening Meinesz-Moritz inverse problem (e.g., Bagherbandi, 2012; Sjoberg, 2009, 2013), the Parker-Oldenburg's method (e.g., Bagherbandi, 2012; Oldenburg, 1974; Shin et al., 2015), and the multiscale gravity analysis method (Xu et al., 2017). Among these methods, the Parker-Oldenburg method has been extensively applied due to its high efficiency (e.g., Block et al., 2009; Gómez-Ortiz & Agarwal, 2005; Prasanna et al., 2013; Shin et al., 2007, 2009, 2015; van der Meijde et al., 2013; Zhang et al., 2015). However, the inherent defects of the fast Fourier transform (FFT) algorithm (i.e., aliasing, edge effects, imposed periodicity, and truncation effect) (Zhao et al., 2018) substantially reduce accuracy of the Parker-Oldenburg method. Recently, Wu and Tian et al. (2014) introduced a Gauss-FFT technique to improve the accuracy of the Fourier transform, which has been applied for calculation of the gravity effect of topography (Wu, 2016).

Since the Bouguer gravity anomalies represent an integrated response to all density variations, their inversion usually provides poor depth resolution. Therefore, using the pure gravity inversion, it is difficult to define correct Moho depths since other factors bias the result (e.g., Kaban et al., 2015). To decrease the nonuniqueness, a joint inversion of gravity with other available geological and geophysical data is usually performed. In particular, seismic data are widely combined with the gravity data to investigate 3-D density structure of the upper mantle (e.g., Deng et al., 2017; Kaban et al., 2014, 2015; Kaban, El Khrepy, et al., 2016), and for the Moho depth inversion (e.g., Baranov et al., 2018; O'Donnell & Nyblade, 2014; Szwillus et al., 2019; Uieda & Barbosa, 2017).

In this study, we adopt a modified version of the Parker-Oldenburg's method to investigate the Moho structure in the Tibetan Plateau and surrounding areas using a joint analysis of the gravity and seismic data. First, detailed equations for the improved Parker-Oldenburg's method are introduced. Then, efficiency of this method is demonstrated by synthetic models. Next, the recent satellite-terrestrial gravity (EIGEN-6C4, Förste et al., 2014), topography (ETOPO1, Amante & Eakins, 2009), and regional/global crustal models (Laske et al., 2013; Stolk et al., 2013) together with seismic tomography (Schaeffer & Lebedev, 2013) are jointly analyzed to estimate Moho depths beneath the Tibetan Plateau. We take into account the most significant effects associated with density heterogeneity of the crust and upper mantle. In the first case, we employ

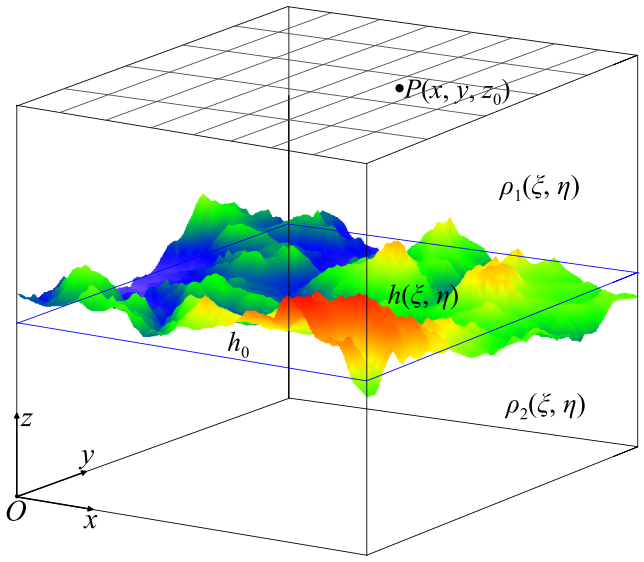

Figure 1. The coordinate system of a synthetic interface and observation points. The vertical z axis is taken to be positive upward.

available crustal models, for example, giving thickness and density of sediments as well as density variations within the crystalline crust. The upper mantle density variations are obtained based on existing tomography models. Finally, we discuss tectonic implications of the estimated Moho variations.

2. Methods

2.1. Gravity Forward Modeling for Moho Topography

We use the Cartesian coordinate system (ξ, η, ζ) for the source body, and (x, y, z) for the observations. As shown in Figure 1, $h(\xi, \eta)$ represents the Moho topography, and h_0 is the regional average Moho depth typically obtained from a priori seismic model. The densities of the upper and lower layers are assumed as $\rho_1(\xi, \eta)$ and $\rho_2(\xi, \eta)$, respectively. The density anomaly due to the Moho undulation is $\rho(\xi, \eta) = \rho_2(\xi, \eta) - \rho_1(\xi, \eta)$. The gravitational potential $U(x, y, z_0)$ at the observation plane z_0 produced by the Moho topography h relative to the average plane h_0 is given by (Blakely, 1996)

$$U(x,y,z_0) = G\int_0^X\int_0^Y\int_{h_0}^{h}\frac{\rho(\xi,\eta)}{R}d\,\xi d\,\eta d\,\zeta, \tag{1}$$

where G is the universal gravitational constant and $R = \sqrt{(x-\xi)^2 + (y-\eta)^2 + (z_0-\zeta)^2}$ is the distance between the observation point $P(x, y, z_0)$ and the source region (ξ, η, ζ). X and Y are the boundaries in the x and y directions, respectively.

The corresponding spectrum expression of the gravitational potential is given by taking 2-D Fourier transform of x and y,

$$\widetilde{U}(k_x,k_y,z_0) = G\int_0^X\int_0^Y\int_{h_0}^{h}\rho(\xi,\eta)\left\{\int_{-\infty}^{+\infty}\int_{-\infty}^{+\infty}\frac{1}{R}e^{-i(k_x x+k_y y)}dxdy\right\}d\,\xi d\,\eta d\,\zeta, \tag{2}$$

where k_x, k_y are wavenumbers in the x and y directions, respectively.

According to the 2-D Fourier transform of the Green's function $1/R$ (Bracewell, 1965) and the translation property of the Fourier transform, equation (2) can be further written as

$$\widetilde{U}(k_x,k_y,z_0) = 2\pi G\int_0^X\int_0^Y\frac{e^{-|k|z_0}}{|k|^2}\rho(\xi,\eta)e^{-i(k_x\xi+k_y\eta)}\left[e^{|k|h}-e^{|k|h_0}\right]d\,\xi d\,\eta, \tag{3}$$

where $k = \sqrt{{k_x}^2 + {k_y}^2}$.

Expanding the exponential terms in square brackets in equation (3) by the Taylor series and taking the vertical derivative, we get a spectrum of the gravity anomalies

$$\Delta\widetilde{g}(k_x,k_y,z_0) = -2\pi G e^{-|k|\cdot z_0}\sum_{n=1}^{\infty}\frac{|k|^{n-1}}{n!}\mathcal{F}\left\{\left[h^n(\xi,\eta)-h_0^n\right]\cdot\rho(\xi,\eta)\right\}, \tag{4}$$

where n is the expansion degree of Taylor series. The symbol F denotes Fourier transform. Equation (4) is the traditional Parker's formula (Parker, 1973). Using this formula may cause inaccurate results because of the aliasing and imposed periodicity as well as edge effects (Wu & Tian, 2014). Furthermore, the exponential function in equation (4) may also cause insufficient computational accuracy, especially when the exponential term$|k|z_0$ is high (Xia & Sprowl, 1995).

Wu (2016) introduced the Gauss-FFT method (Wu & Tian, 2014) to improve accuracy of the Parker's formula. Instead of the rectangular quadrature, the Gaussian quadrature is used in each integral interval,

which increases the computational accuracy more than two orders of magnitude compared with the traditional FFT method (Zhao et al., 2018). The 2-D Gauss-FFT with four nodes is used in this study.

Furthermore, to increase the stability of the exponential term, we shift the exponential terms in equation (3) to the average depth of the Moho topography (h_0) instead of 0 in the traditional Parker's formula equation (4), which gives

$$\Delta\widetilde{g}(k_x,k_y,z_0) = -2\pi G e^{-|k|(z_0-h_0)}\sum_{n=1}^{\infty}\frac{|k|^{n-1}}{n!}\mathcal{F}\{[h(\xi,\eta)-h_0]^n\cdot\rho(\xi,\eta)\}. \tag{5}$$

2.2. Gravity Inversion for the Moho Topography

According to Oldenburg (1974), we rearrange equation (5), giving

$$\mathcal{F}\{[h(\xi,\eta)-h_0]\cdot\rho(\xi,\eta)\} = -\frac{\Delta\widetilde{g}e^{|k|(z_0-h_0)}}{2\pi G} - \sum_{n=2}^{\infty}\frac{|k|^{n-1}}{n!}\mathcal{F}\{[h(\xi,\eta)-h_0]^n\cdot\rho(\xi,\eta)\}, \tag{6}$$

when h_0 and $\rho(\xi,\eta)$ are known, $h(\xi,\eta)$ can be calculated iteratively using equation (6) with three steps: (1) the most recent determination of $h(\xi,\eta)$ is used to evaluate the right-hand side of equation (6); for the first iteration, $h(\xi,\eta)$ is commonly set to be 0; the inverse Fourier transform of the left-hand side of equation (6) gives an updated value of the Moho topography; the iterative procedure is continued until some convergence criterion is met or a maximum iteration number is reached.

To improve convergence and stability of the computation, the recurrence formulas are modified according (Feng et al., 1986):

$$\mathcal{F}\{[h(\xi,\eta)-h_0]\cdot\rho(\xi,\eta)\} = -\tau\cdot\frac{\Delta\widetilde{g}}{2\pi G}e^{|k|(z_0-h_0)}, \tag{7}$$

where the factor τ is introduced to correct the effects of the deleted terms in equation (6). It commonly ranges from 0.8 to 0.95 (Feng et al., 1986).

It is worth noting that the term $\Delta\widetilde{g}e^{|k|(z_0-h_0)}$ is numerically equivalent to the downward continuation of the gravity data to the depth ($z_0 - h_0$). This may lead to unstable results due to the short-wavelength components associated with noise multiplied by large exponential factors (Oldenburg, 1974). Therefore, the straightforward application of the iterative procedure usually results in a divergent solution characterized by high-frequency oscillations (Oldenburg, 1974). In order to reduce the short wavelength oscillations in the downward continuation, a low-pass cosine filter $B(k)$ is used in this study (Nagendra et al., 1996; Shin et al., 2007)

$$B(k) = \begin{cases} 1 & |k|<WH \\ \frac{1}{2}\left\{1+\cos\left[\frac{\pi(k-WH)}{SH-WH}\right]\right\} & WH\le|k|\le SH \\ 0 & |k|>SH \end{cases}, \tag{8}$$

where WH and SH are given frequencies. The value of WH is about half of SH (O'Donnell & Nyblade, 2014; Steffen et al., 2011). This filter cuts off all frequencies higher than SH and entirely passes the frequencies lower than WH, while the frequencies between them are partly passed.

2.3. Joint Analysis of Gravity and Seismic Data

To mitigate the nonuniqueness of the gravity inversion, the seismic-inferred Moho values are used as prior information to determine the optimized parameters (the reference depth h_0 and the density contrast ρ) by searching the maximum correlation coefficient between the gravity-inverted results and the seismic data.

The correlation coefficient γ_c is calculated following (Lawrence & Lin, 1989)

$$\gamma_c = \frac{2S_{12}}{S_1^2 + S_2^2 + \left(\overline{Y}_1 - \overline{Y}_2\right)^2}, \tag{9}$$

where

$$\begin{aligned} &\overline{Y}_j = \frac{1}{N}\sum_{i=1}^{N} Y_{ij}, \;\; S_j^2 = \frac{1}{N}\sum_{i=1}^{N}\left(Y_{ij} - \overline{Y}_j\right)^2, \;\; j = 1, \;\; 2; \\ &S_{12} = \frac{1}{N}\sum_{i=1}^{N}\left(Y_{i1} - \overline{Y}_1\right)\left(Y_{i2} - \overline{Y}_2\right), \end{aligned} \tag{10}$$

where Y_1 represents the gravity-estimated Moho depth; Y_2 represents the seismic-inferred Moho; N denotes the number of the data.

3. Synthetic Examples

In this section, we perform tests on a synthetic Moho model to examine the accuracy of the improved Parker's method with the Gauss-FFT technique. An artificial inversion example is carried out, and we test the effects of the inversion parameters (the reference depth and density contrast).

3.1. Forward Modeling

The synthetic Moho model $h(\xi, \eta)$ is shown in Figure 2a. This model extends horizontally from 0 to 2048 km and is divided into 256 grid nodes with a constant interval of 8 km in both x and y directions. The reference Moho depth is set to be $h_0 = 30$ km with the density contrast $\rho = 400$ kg/m^3. The observation plane is at $z_0 = 0$ km with the same discretization as the source.

The gravity anomalies at the z_0 plane are computed by the spatial forward method, in which the Moho model is discretized into small prisms, and then the gravity effect of each prism is calculated and superposed (e.g., Blakely, 1996; Li & Chouteau, 1998) as shown in Figure 2b. The gravity anomalies computed by the traditional Parker's formula (equation (4)) and the improved Parker's equation (equation (5)) with the Gauss-FFT are shown in Figures 2c and 2d, respectively. The differences relative to the theoretical values are shown in Figures 2e and 2f.

As shown in Figure 2, the main features of the gravity anomalies derived from the traditional Parker's formula (Figure 2c) are similar to the theoretical solution (Figure 2b), while the maximum absolute errors are about 13 mGal at the boundaries where the Moho topography changes rapidly (Figure 2e). In contrast, the gravity anomalies derived from the improved Parker's formula (Figure 2d) are almost the same as the analytical solution, with the maximum absolute error less than 0.25 mGal (Figure 2f), which implies that the results obtained from the improved Parker's formula are more precise.

3.2. Synthetic Inversion Test

In the Parker-Oldenburg inversion, the reference depth h_0 and the density contrast ρ have significant impacts on the inversion results (O'Donnell & Nyblade, 2014). In this section, the influence to these parameters is tested, and the correlation coefficients are calculated to determine the most appropriate parameters. The synthetic forward model in Figure 2a is adopted as the true model and the gravity anomalies in Figure 2d are considered as the observation data in the inversion. The improved Parker's formula associated with four nodes Gauss-FFT method is used in the Parker-Oldenburg inversion.

We test the influences of the reference depth h_0 and the density contrast ρ, respectively. By changing the value of h_0 and keeping ρ equal to its original value, we obtain the results on the profile AA′ as shown in Figure 3a. Figure 3a demonstrates several Moho profiles for five reference depths. This test demonstrates the strong nonuniqueness of the gravity inversion, these solutions with different reference depth h_0 can equally fit the observation data. The test also shows that the inverted Moho interface has more short-wavelength undulations as the reference depth increases. Similarly, a range of the density contrast ρ is tested for the same (actual) h_0 as shown in Figure 3b. This test shows that the observation data can be also fitted by applying different density contrasts. The Moho depth is underestimated when the density contrast is higher than the actual one and vice versa.

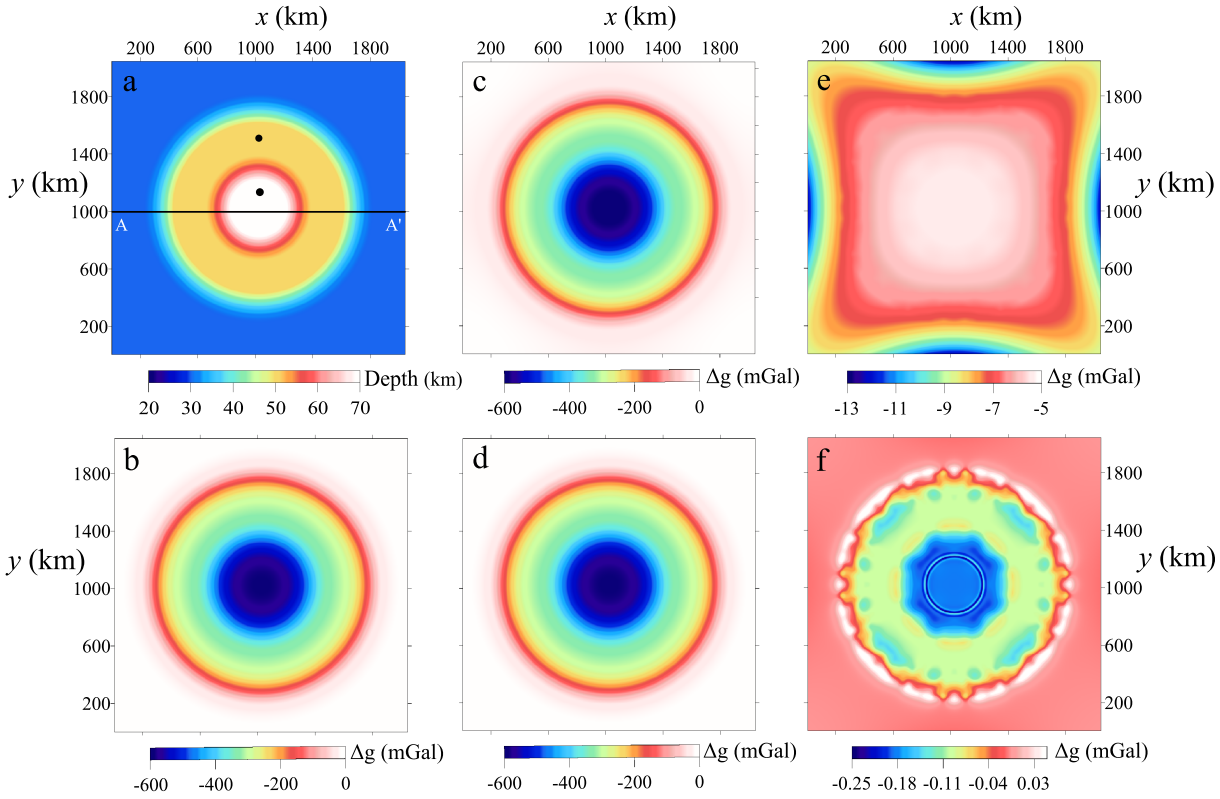

Figure 2. The synthetic Moho model and its gravity anomalies. (a) The Moho depth of the model; (b) the theoretical gravity anomalies caused by the modeled Moho observed at zero level; (c) and (d) are the gravity anomalies obtained from the traditional Parker's formula and from the improved one, respectively; (e) and (f) are their differences from the analytical solution (b). The AA′ in Figure 2a indicates the location of the cross section in Figures 3 and 4, and the points show the locations where the Moho values are used as a priori information in the correlation analysis in section 3.2.

To reduce the nonuniqueness of the inversion, we use the correlation method described in section 2.3 to determine the best combination of h_0 and ρ. The Moho depths for two locations (black dots in Figure 2a) are given as prior information to calculate the correlation coefficients γ_c. A range of the reference depths h_0 and density contrasts ρ are investigated. The distribution of correlation coefficients and the inversion results along the profile AA′ are shown in Figures 4a and 4b.

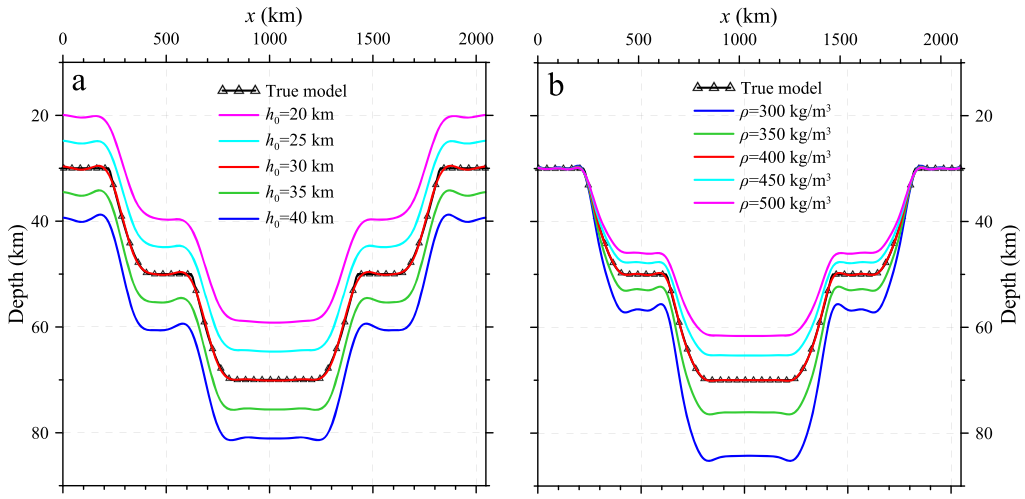

Figure 3. The inverted Moho undulations for the synthetic model in Figure 2a based on different reference depths (a) and density contrasts (b).

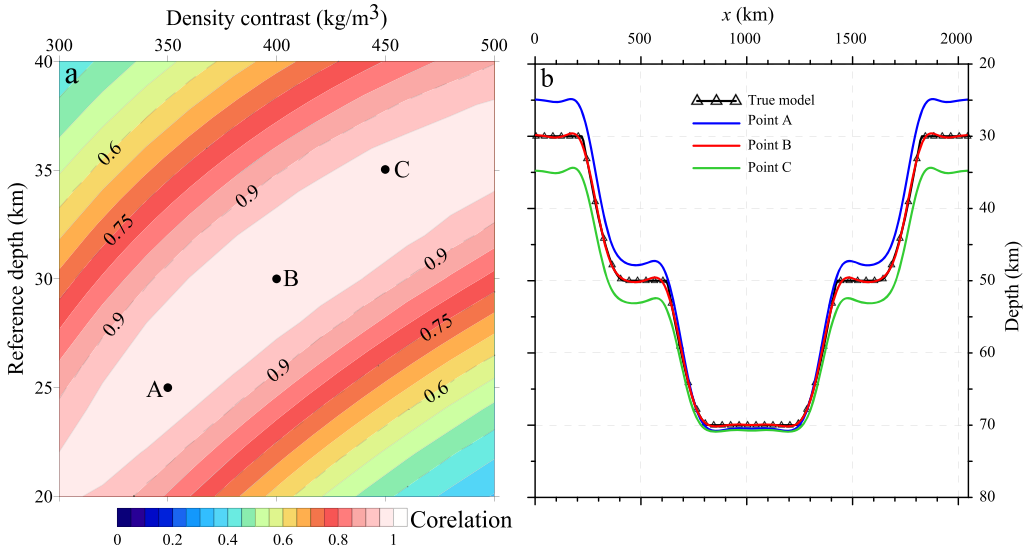

Figure 4. Distribution of the correlation coefficients (a) and the inversion results on the profile AA′ (b) derived by the parameter combinations of points A, B, and C in (a).

In Figure 4a, the maximum correlation is found to be 0.99 at Point B, where the reference depth and the density contrast are $h_0 = 30$ km, $\rho = 400$ kg/m^3. The values coincide well with the true model. Points A and C have relatively high correlations with $h_0 = 25$ km, $\rho = 350$ kg/m^3 and $h_0 = 35$ km, $\rho = 450$ kg/m^3, respectively, but the inverted Moho depths are shallower or deeper than the actual model as shown in Figure 4 b. This model test indicates that a priori information (e.g., seismic Moho) can be easily combined to constrain the determination of the parameters in the gravity inversion.

4. Moho Structure of the Tibetan Plateau

4.1. Data

The EIGEN-6C4 model (Förste et al., 2014, http://icgem.gfz-potsdam.de/tom_longtime) to degree and order 720 is used to compute the free-air gravity disturbances at the elevation 10 km refer to the GRS80 reference ellipsoid (Figure 5b). The gravity effects (Figure 5c) of the topography (Figure 5a) derived from ETOPO1 (Amante & Eakins, 2009) are calculated globally (Zhao et al., 2019) with the correction density of 2,670 kg/m^3. The Bouguer gravity disturbances (Figure 5d) are obtained by removing the gravity effect of the topography from the free-air gravity disturbances.

The Bouguer gravity disturbances mainly reflect the effects of crustal density heterogeneities (sediments and crystalline crust), variations of the Moho boundary, and upper mantle density variations. The effect of the deep mantle is characterized by very small changes in the limited area of Tibet with surroundings and is insignificant for this study (Kaban, Stolk, et al., 2016). Ideally, the gravity effects of the sedimentary layer, crystalline crust, and upper mantle should be removed from the Bouguer gravity disturbances to refine the gravity anomalies produced by the Moho topography. In this study, the crust model of Asia (Stolk et al., 2013) is used to calculate the gravity corrections for the entire Earth after embedding this regional model in the global crustal model CRUST1.0 (Laske et al., 2013). The gravity effect of the sedimentary layer (Figure 6a), which is calculated relative to the density 2700 kg/m^3, is taken from Kaban, Stolk, et al. (2016). The effects of the three crystalline crust layers are calculated down to the Moho relative to the average density in each of them (Tenzer et al., 2009; Tenzer, Chen, Tsoulis, et al., 2015); the total effect is shown in Figure 6b. The effect of the upper mantle from the Moho down to 325 km (Figure 6c) is computed based on the global tomography model SL2013sv of Schaeffer and Lebedev (2013). The velocity variations were converted into density variations using a mineral physics approach as in (Kaban, Stolk, et al., 2016). All these fields are calculated at the 10 km elevation. The final residual anomalies (Figure 6d) are obtained by removing all these effects from the Bouguer gravity disturbances (Figure 5d). We note that the lower boundary for

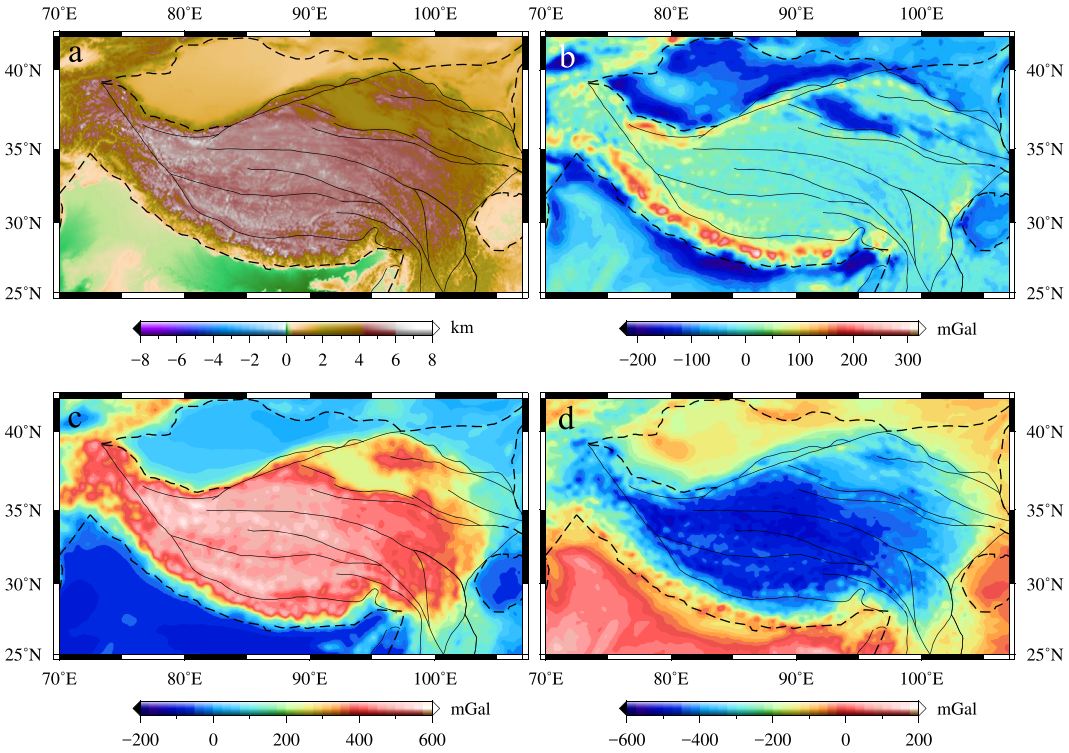

Figure 5. (a) Topography of the Tibetan Plateau; (b) Free-air gravity disturbances from the EIGEN-6C4 model; (c) gravity effects of the topography; (d) Bouguer gravity anomalies.

the crustal density correction is the Moho boundary; therefore, any change of the Moho would have an effect on the crystalline crust correction (Tenzer & Chen, 2019). Therefore, we performed an iterative procedure to take into account possible changes of the Moho. Based on the Moho results of the first iteration, we re-estimated the gravity effect of the crystalline crust with the new Moho and calculated new residual gravity disturbances used in the Moho inversion. The new gravity disturbances are used to obtain the Moho for the second iteration. The difference with the first iteration is much less (approximately 8 times) than the difference with the initial model; therefore, convergence can be easily reached. The iterative process is repeated until the convergence is reached. Further details are described in the supporting information.

4.2. Moho Structure Beneath Tibet

As shown in section 3.2, the reference depth and density contrast strongly influence the amplitude and pattern of the gravity-inverted results. Here, the Moho density contrast is defined as the average density contrast between the crust and upper mantle. To reduce the nonuniqueness of the gravity inversion, we employ the initial seismic-determined Moho depths (Stolk et al., 2013) as constraints to obtain an appropriate set of the reference depth and Moho density contrast in the gravity inversion. The locations of the Moho determinations compiled by Stolk et al. (2013) are shown in Figure 7.

We determine the best values of the parameters by searching for the maximum correlation between the gravity-inverted results and the seismic-derived Moho. A range of the reference depths between 30 and 60 km and the range of the density contrast 300 kg/m^3 to 900 kg/m^3 are analyzed to calculate the correction coefficients shown in Figure 8a. Figure 8b shows the differences between the inverted Moho depths and seismic determinations (Figure 7). The resulted Moho depths obtained in the inversion are shown in Figures 9a and 10.

As shown in Figure 8a, the maximum correlation coefficient reaches 0.82 when $h_0 = 48$ km and $\rho = 580$ kg/m^3. This set of parameters is different from previous studies, for example, 50 km and 480 kg/m^3 in Xu et al.

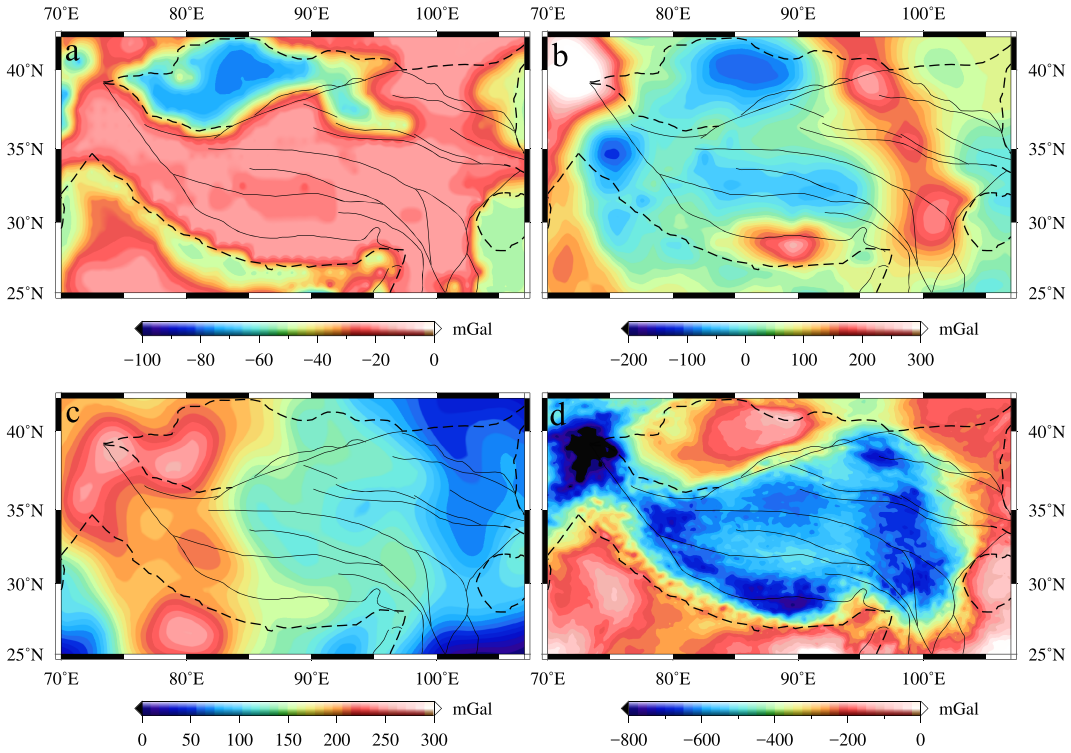

Figure 6. Gravity effects of (a) sedimentary layers, (b) crystalline crust layers, and (c) upper mantle down to 325 km (Kaban, Stolk, et al., 2016). (d) The residual gravity disturbances calculated by removing the effects (Figures 6a–6c) from the Bouguer gravity disturbances (Figure 5d).

(2017), 48 km and 600 kg/m^3 for land while 500 kg/m^3 for ocean in Bagherbandi (2012), and 32 km and 368 kg/m^3 in Shin et al. (2009). The distribution of the seismic determinations of Stolk et al. (2013) used in this study is very inhomogeneous. The Moho determinations are sparse in the southwestern Tibet and dense in the eastern part of the study area. The different seismic data coverage may affect the optimal ρ and h_0 and eventually affect the inverted results. We performed two additional experiments using different

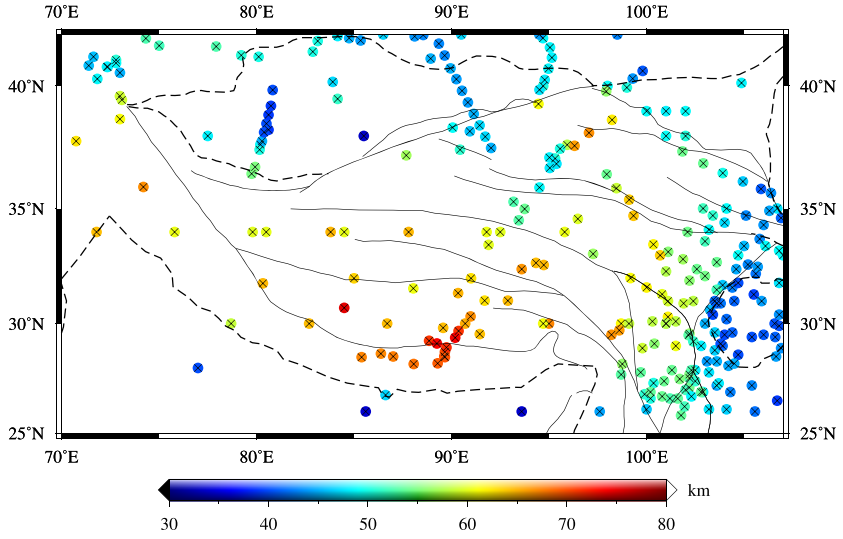

Figure 7. The Moho depth of the Tibetan Plateau based on the existing seismic determinations compiled by Stolk et al. (2013). Crosses show location of the original seismic data.

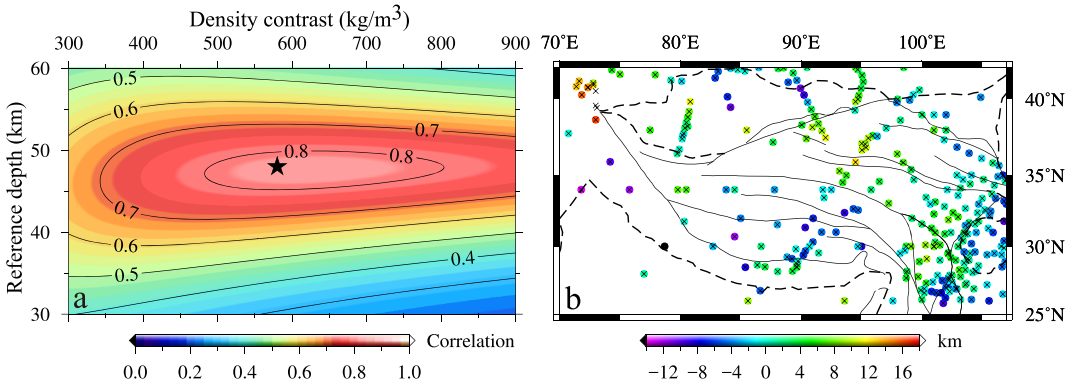

Figure 8. (a) Correlation coefficients between the Moho depths from Stolk et al. (2013) and our inversion results. (b) Difference between the Moho depths from Stolk et al. (2013) and the inverted Moho for the parameters providing the best correlation with the seismic estimates ($h_0 = 48$ km and $\rho = 580$ kg/m^3 marked by a star in Figure 8a).

constraints using separated data points from the western and eastern half of the whole area in Figure 7 (see the supporting information). These tests show that the main features of the results constrained by different data sets are qualitatively similar; however, there exists a difference of the amplitudes (the maximum difference compared to the inverted Moho depth in Figure 9a is less than 5 km).

Furthermore, the area of the maximum correlation is extended for a broad range of the density contrast. For example, the correlation 0.8 fits to a range of 500–700 kg/m^3 in this model (Figure 8a). Two additional tests using the extreme parameter combinations are carried out for $\rho = 500$ kg/m^3, $h_0 = 47$ km in the first test and for $\rho = 700$ kg/m^3, $h_0 = 48$ km in the second test (see the supporting information). As demonstrated by these tests, the main features of the results remain nearly the same as for the model in Figure 10, but the Moho variations are relatively larger in amplitude in the first test, or lower in the second one due to the great difference of the density contrast (200 kg/m^3). The maximum difference of the inverted Moho depths in these extreme tests is about 7.5 km, which can be interpreted as the sensitivity limit (or uncertainty) of the correlation-based joint inversion of the gravity and seismic data.

As shown in Figures 7 and 8b, there are 274 seismic-derived Moho values used in the correlation analysis. In Figure 8b, there are 175 points (~63.8%) with the difference less than 5 km. The locations with gaps larger than 10 km only occupy ~8.4% (23 points), and the mean square difference between the inverted results and the Moho depths from Stolk et al. (2013) is 0.91 km. Therefore, the inverted results well correspond to the seismic estimations of the Moho depth. The maximum difference is about 20.1 km at the location (39°N, 73°E), located in the western Tibet with low seismic coverage. It should be noted that in areas of the continental collision, seismic determinations often give controversial results, which may correspond to different colliding plates and the Moho of the subducting plate would be deeper than of the obducting one (e.g., Mechie et al., 2011; Mechie & Kind, 2013). Therefore, we should not expect full correspondence of different results. The differences may also stem from (1) the uncertainties of the Asian crustal model (Stolk et al., 2013) used for the sedimentary and crystalline crust corrections; (2) the relatively low resolution of the crustal model, which may lead to losing short-wavelength signals; and (3) uncertainties and low resolution of the seismic tomography model used to calculate the upper mantle gravity anomaly. The conversion between seismic velocity and density may be biased by several factors, such as composition (Kaban, Stolk, et al., 2016).

Some major features of the obtained Moho depth variations are different from other published results based on the gravity data (e.g., Baranov et al., 2018; Braitenberg et al., 2000, 2003; Chen & Tenzer, 2017; Shin et al., 2015; Tenzer et al., 2013; Xu et al., 2017). For comparison, the interpolated seismic-derived Moho (Stolk et al., 2013) and four most recent results (Baranov et al., 2018; Chen & Tenzer, 2017; Shin et al., 2015; Xu et al., 2017) are shown in Figures 9b–9f. Our results (Figure 9a) reveal that the Moho is quite deep in southern Tibet along the Indus-Tsangpo Suture (ITS) (75–77 km), and relatively deep Moho is also observed in northern and eastern Tibet in the Songpan-Ganzi Block (SGB) (65–67 km). The maximum Moho depth ~79 km is found in Karakorum and in the southern Lhasa block along the ITS. The different Moho topography was also

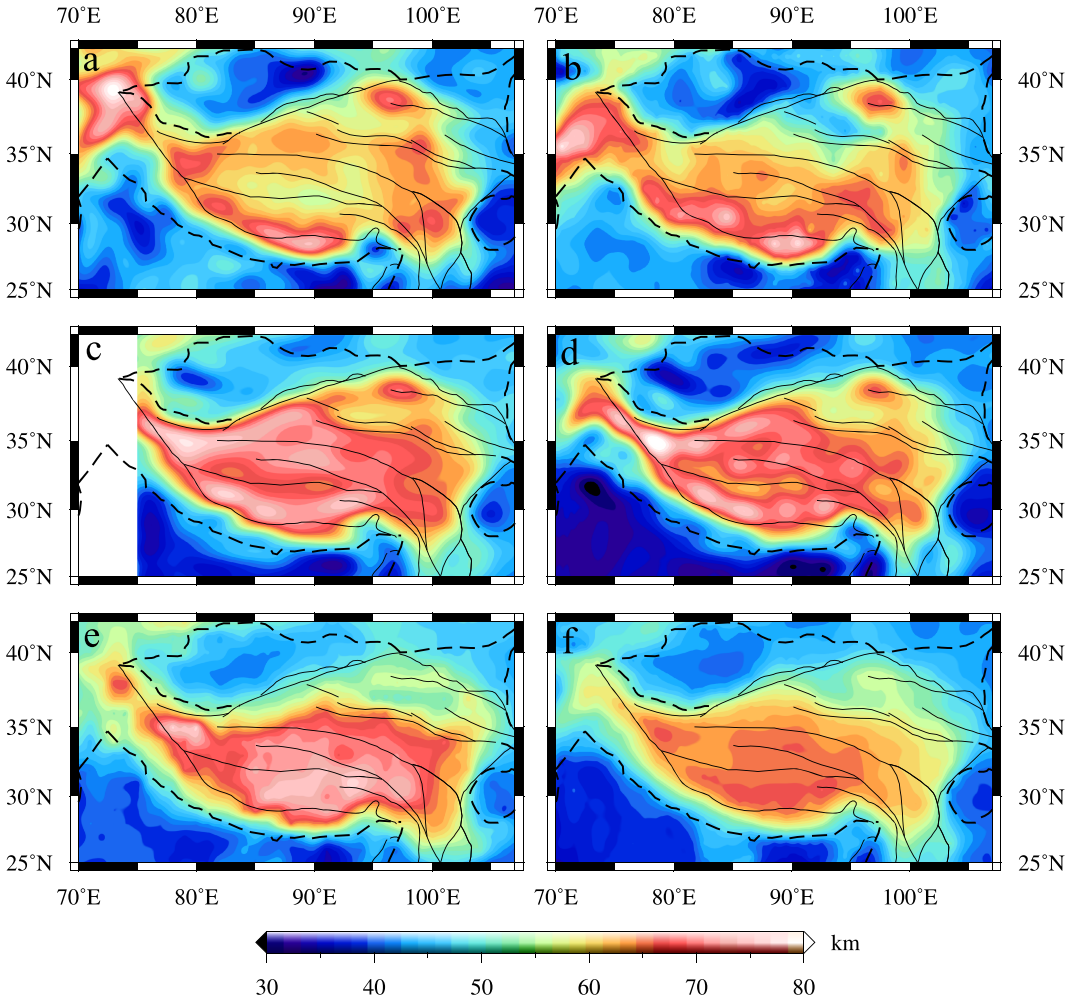

Figure 9. Comparison of Moho models derived by (a) our results; (b) Stolk et al. (2013); (c) Xu et al. (2017); (d) Shin et al. (2015); (e) Baranov et al. (2018); and (f) Chen and Tenzer (2017). Note that there is no data in 70–75°E in Xu et al. (2017).

reported by Shin et al. (2015) and Xu et al. (2017). Their models reveal the deep Moho (72–75 km) in northern Tibet along the margins with the Tarim basin and the Himalayas with the maximum Moho depth 77 (Xu et al., 2017) and 79.5 km (Shin et al., 2015) in western Tibet. Baranov et al. (2018) reported that the deep Moho (65–74 km) occurs under the Lhasa terrane and under Taksha at the Karakoram fault, with the maximum Moho deepening to ~76 km in the south of the Bangong-Nujiang suture under the Lhasa terrane. According to the results of Chen and Tenzer (2017), the relatively deep Moho (65–70 km) is observed beneath western and central Tibet, and the maximum Moho depth ~71 km is found under the ITS.

Noticeable differences also occur in the northwestern and central Tibet, as shown in Figure 9. For example, in the central Tibet, the visible shallow region is observed in the Lhasa Block and Qiangtang Block crossed by the Bangong-Nujiang Suture (BNS) in Shin et al. (2015), Xu et al. (2017), and our results, but this feature is not observed in the results of Chen and Tenzer (2017), Stolk et al. (2013), and Baranov et al. (2018). In the northwestern Tibet, around the Karakorum, the Moho deepens to 70–80 km in our result, which coincides with the receiver function results beneath the Pamir (Schneider et al., 2013) and the seismic-derived Moho model (Stolk et al., 2013), while the Moho is not so deep according to Baranov et al. (2018), Shin et al. (2015), and Chen and Tenzer (2017). Compared to the seismic-derived Moho model of Stolk et al. (2013), we found that the pattern of our inverted Moho is much closer to the seismically derived map than of the previous results obtained from the gravity data (e.g., Baranov et al., 2018; Chen & Tenzer, 2017; Shin et al., 2015; Xu et al., 2017) as shown in Figure 9.

Several factors may be responsible for the differences among these gravity-derived Moho models. First of all, in the studies of Bagherbandi (2012), Shin et al. (2007, 2009, 2015), and Xu et al. (2017), the Bouguer gravity anomalies were used in the inversion; therefore, these results are biased by the effects of the mass variations in the sedimentary layer, crystalline crust and upper mantle. Although the gravity effects of the sedimentary and crystalline crust layers have been removed from the Bouguer gravity anomalies in the studies of Baranov et al. (2018) and Chen and Tenzer (2017), these studies did not remove the gravity effect of the mass anomalies in the upper mantle, which is significant with the amplitude reaching 300 mGal (Figure 6c). Thus, the persisting gravitational signal of mantle heterogeneities could introduce large systematic bias into the gravimetric Moho determinations (Tenzer, Chen, Tsoulis, et al., 2015). Also, the gravity effect of the crystalline crust estimated in these studies is based on the model CRUST1.0, which provides extremely low resolution for these parameters. In this study, the gravity effects of mass anomalies of the sediment layers, the crystalline crust, and the upper mantle are removed from the Bouguer gravity anomalies, which ideally should guarantee that the resulting gravity anomalies used in the inversion are mainly due to the Moho undulation. Unfortunately, the available crustal and mantle models also contain large uncertainties. Furthermore, the available seismic-derived Moho data are applied as constraints in the gravity inversion, which dramatically reduced the nonuniqueness and provided the more reliable Moho model.

4.3. Results and Discussions

Our results show that the Moho structure beneath the Tibetan Plateau is very complicated (Figure 10). In the Indian shield and Ganges basin, the Moho is shallow with a depth of 30–45 km. Here, the shallowest Moho is observed in the northwest and the northeast of the Ganges basin, and south of the Main Frontal Thrust (MFT). The Moho dips gently from the depths 40–45 km on the Indian plate to about 50 km beneath the southern Himalayas, which is consistent with previous gravity/seismic studies (Shin et al., 2007, 2009, 2015; Stolk et al., 2013; Teng et al., 2013, 2014; Xu et al., 2017).

Northward, the Moho deepens more rapidly in the northern Himalayas, reaching a depth of ≥70 km north of the Indus-Tsangpo Suture (ITS) in the southern Lhasa block. The deeper Moho feature appears as a "Moho depression belt" in the southern Lhasa block and the northern Himalayas. It is approximately parallel along the ITS, and extends from 77°E in the west, to 93°E in the east, and reaches up to 75–80 km between 85°E and 90°E. It also corresponds to the deepest subduction location of the Indian plate beneath southern Tibet as revealed by seismic studies (e.g., Nábělek et al., 2009; Shi et al., 2016).

In central Tibet, the Moho becomes relatively shallow under the northern LSB and southern Qiangtang block (QTB) (55–60 km, Figure 10). The minimum depth (~55 km) is observed beneath the Bangong-Nujiang Suture (BNS) around the longitude of 90°E. The shallower Moho is typical for central Tibet, and it becomes deeper (65–70 km) in the eastern and western QTB. Further to the north, the Moho in the SGB is located at a depth of 60–65 km, which is deeper than beneath the QTB, but shallower than in the "Moho depression belt" beneath the southern LSB. Here we observe another "Moho depression belt" located beneath the SGB, extending from the West Kunlun Fault (WKLF) in the west, along the northern margin of Tibet at the boundary with the Tarim basin to the Xianshuihe-Xiaojiang Fault (XSF-XJF) in the east, although it is not entirely continuous beneath the SGB.

The two visible "Moho depression belts" are marketed by blue dashed lines in Figure 10. They are characterized by the increased Moho depths up to 65–75 km, while between them the Moho depth is shallower (about 55–65 km) in central Tibet, forming a basin shape feature. The southern "Moho depression belt" is formed in a compressional environment, where the Indian plate underthrusts northward beneath the Tibetan Plateau. This belt-like feature fits well to the results of the seismic experiment (INDEPTH) (Zhao et al., 2011), and to the seismological observations along the Lhasa-Golmud transect (Mechie & Kind, 2013). The northern "Moho depression" is shallower than the southern one, which is also in good agreement with previous seismic profile studies (e.g., Mechie & Kind, 2013; Zhao et al., 2011).

Several mechanisms have been suggested to explain the complicated Moho variations in Tibet. The maximum Moho depths along the Himalayas and along the northern margin of Tibet at the boundary with the Tarim basin have been interpreted by the continental subduction (e.g., Kind et al., 2002; Kumar et al., 2006; Mechie & Kind, 2013;Willett & Beaumont, 1994 ; Zhao et al., 2011). Another model proposes more complex Moho geometry under Tibet with the maximum under the Lhasa domain, which could be explained by

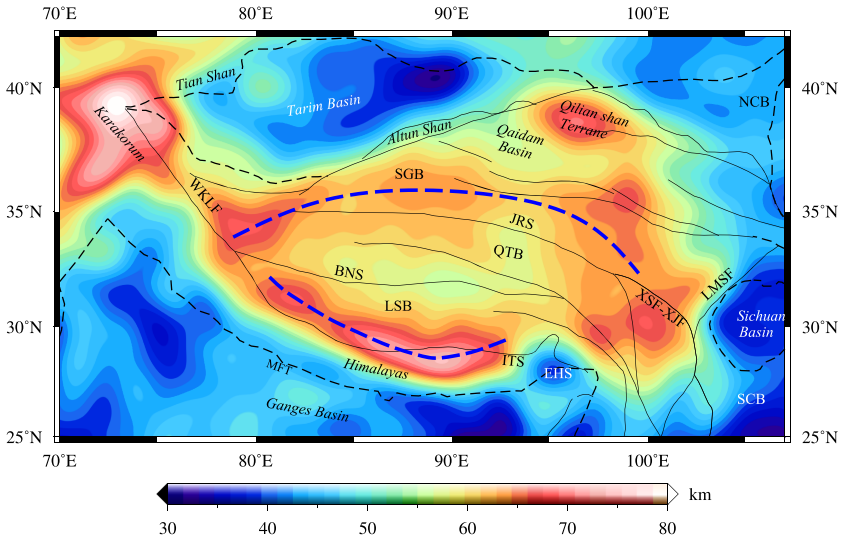

Figure 10. The inverted Moho topography after the joint inversion with the seismic-estimated Moho depth. Abbreviations are as follows: MFT, Main Frontal Thrust; ITS, Indus-Tsangpo Suture; LSB, Lhasa Block; BNS, Bangong-Nujiang Suture; EHS, Eastern Himalaya Syntaxis; EKLF, East Kunlun Fault; QTB, Qiangtang Block; SGB, Songpan-Ganzi Block; LMSF, Longmenshan Fault; NCB, North China Block; XSF-XJF, Xianshuihe-Xiaojiang Fault; SCB, South China Block; WKLF, West Kunlun Fault. Two blue dashed lines represent two main "Moho depression belts."

interaction of several tectonic blocks that are broken and tilted (e.g., Tapponnier et al., 2001). Alternative models also suggest that the India plate subsides far north under central (and even northern) Tibet (e.g., Tilmann et al., 2003; Zhao et al., 2011). Moreover, the extrusion or escape mechanism (e.g., Tapponnier et al., 2001) and the lower crustal flow (e.g., Royden et al., 1997, 2008) were also suggested to explain the complex Moho structure in eastern Tibet.

We also interpret the deep "Moho depression belt" along the ITS as a result of the underthrusting of the Indian lithosphere beneath Tibet, which is supported by the Hi-CLIMB experiment (Nábělek et al., 2009), which shows that the Moho is dipping gently from a depth of 40 km beneath the Ganges Basin within the Indian Plate to 50 km beneath the Himalayas, and the lower part of the Indian lithosphere northward underplates Tibet up to 31°N reaching a depth of 70 km north of the ITS, which is in a good agreement with the deep "Moho depression belt" near the ITS according to our model. Due to the continuous convergence of the Indian plate, the bottom of the crust beneath the southern Tibet (south of the ITS) is dipping to the north, whereas that one beneath the Lhasa block (north of ITS) is dipping to the south, forming the deep "Moho depression belt" along the ITS.

On the other hand, the relatively deep "Moho depression belt" beneath the northern Tibet can be explained by the reverse subduction of the rigid Asian lithosphere (Willett & Beaumont, 1994; Zhao et al., 2011). The recent seismic experiment INDEPTH IV (e.g., Zhao et al., 2011) has revealed a relatively thin Tibet lithosphere overriding the southward subducting Asian lithosphere beneath northern Tibet, which could explain the relatively thick Moho in northern Tibet. Besides, the northward motion of the Indian subcontinent that followed the onset of continental collision with Asia has produced extensive deformation in the Tibet area (Yin & Harrison, 2000). Owing to the relatively rigid lithosphere of the Tarim basin in the west, Qaidam basin in the north and Sichuan basin in the east (Chen et al., 2013, 2015), large deformations have been localized in the relatively weak lithosphere of the Songpan-Ganzi block (Chen et al., 2015) near the boundaries of the rigid blocks, resulting in the crust thickening as well as in the northern "Moho depression" in Tibet. Between these two Moho depressions, the relative shallower Moho depth in the central Tibet may indicate that this region is isostatically compensated by the lower-velocity (and consequently, by low density) mantle (Kind et al., 2002; Nábělek et al., 2009).

In northern Tibet, the Moho is relatively shallow in the Qaidam Basin across the East Kunlun Fault (EKLF) with a depth of 55–60 km, while it deepens to 68–70 km in the Qilian Shan. The Moho is

about 30–50 km in the Tarim Basin. It is also evident that the Moho depth in the eastern Tarim Basin (32–40 km) is relatively shallower than in the western (40–50 km), which also coincides with the seismic-derived Moho map (Stolk et al., 2013). In the east of Tibet, the Moho depth is quite shallow and located at a depth of 35–40 km in the Sichuan Basin. These results are a good agreement with previous Moho results (Chen & Tenzer, 2017; Shin et al., 2015; Stolk et al., 2013; Xu et al., 2017). Furthermore, the extremely deep Moho (70–80 km) is observed beneath the Karakoram fault region, which might be related to the deep subduction of the continental lithosphere beneath the Pamir (Burtman & Molnar, 1993; Schneider et al., 2013).

5. Conclusions

In this work, we applied the improved Parker-Oldenburg method combined with the seismic determinations to investigate the Moho structure beneath the Tibetan Plateau. The Gauss-FFT method was adopted to improve the traditional Parker's formula. The synthetic forward model shows that the accuracy of the modified formula is principally improved. This method was then applied in the inversion for determination of the Moho depths based on gravity data. To reduce nonuniqueness of the gravity inversion, we used a priori seismic information to determine the best inversion parameters (the reference depth and density contrast) by searching for the maximum correlation between the gravity-inverted results and seismic data.

Comparing to previous studies employing the gravity inversion, the effect of the upper mantle has been computed based on the seismic tomography model and removed from the observed fields. We have also calculated and removed the effects of sediments and crystalline crust based on available crustal models. As a result, the inverted Moho depths are much close to the seismic-based models than those obtained in previous studies based on the gravity inversion.

The inversion results show that the Moho structure under the Tibetan Plateau is very complex with the depths varying from 30–40 km in the surrounding basins to 60–80 km in the plateau. Two distinct "Moho depression belts" are found in the Lhasa and Qiangtang terranes, which are also in good agreement with seismic studies. The southern "Moho depression belt" might be formed as a result of the northward underthrusting of the Indian plate beneath the Tibetan Plateau, while the northern one is interpreted as the subduction of the Asian lithosphere.

Some factors possibly affecting the inverted results may be improved in the future. The seismic-Moho determinations compiled by Stolk et al. (2013), which are used in this study, are very inhomogeneous: sparse in southwestern Tibet and dense in the eastern part. Therefore, the correlation in the area with higher data density strongly influences the inverted results in other areas, which might bias the inversion. Future seismic determinations in western Tibet would provide more reliable constraint to the gravity inversion.

Acknowledgments
The authors thank the Editor Thorsten Becker and two anonymous reviewers for their helpful comments that have greatly improved this paper. This research is supported by the National Natural Science Foundation of China (Grants 41404061, 41674080, and 41674079), the Fundamental Research Funds for the Central Universities of Central South University (2019zzts077), and the scholarship from China Scholarship Council (CSC, 201806370058). The data and codes for this paper are available at the website: https://doi.org/10.6084/m9.figshare.9891662.v1.

References

Amante, C., & Eakins, B. W. (2009). ETOPO1 arc-minute global relief model: Procedures, data sources and analysis.

Audet, P., & Burgmann, R. (2011). Dominant role of tectonic inheritance in supercontinent cycles. *Nature Geoscience*, *4*(3), 184–187. https://doi.org/10.1038/ngeo1080

Bagherbandi, M. (2012). A comparison of three gravity inversion methods for crustal thickness modelling in Tibet plateau. *Journal of Asian Earth Sciences*, *43*(1), 89–97. https://doi.org/10.1016/j.jseaes.2011.08.013

Baranov, A., Bagherbandi, M., & Tenzer, R. (2018). Combined gravimetric-seismic Moho model of Tibet. *Geosciences*, *8*(12), 461. https://doi.org/10.3390/geosciences8120461

Blakely, R. J. (1996). *Potential theory in gravity and magnetic applications*. Cambridge: Cambridge University Press.

Block, A. E., Bell, R. E., & Studinger, M. (2009). Antarctic crustal thickness from satellite gravity: Implications for the Transantarctic and Gamburtsev Subglacial Mountains. *Earth and Planetary Science Letters*, *288*(1-2), 194–203. https://doi.org/10.1016/j.epsl.2009.09.022

Bracewell, R. (1965). Pentagram notation for cross correlation. In *The Fourier transform and its applications* (Vol. 46, p. 243). New York: McGraw-Hill.

Braitenberg, C., Wang, Y., Fang, J., & Hsu, H. T. (2003). Spatial variations of flexure parameters over the Tibet–Quinghai plateau. *Earth and Planetary Science Letters*, *205*(3-4), 211–224. https://doi.org/10.1016/S0012-821X(02)01042-7

Braitenberg, C., Zadro, M., Fang, J., Wang, Y., & Hsu, H. T. (2000). The gravity and isostatic Moho undulations in Qinghai–Tibet plateau. *Journal of Geodynamics*, *30*(5), 489–505. https://doi.org/10.1016/S0264-3707(00)00004-1

Burtman, V. S., & Molnar, P. H. (1993). *Geological and geophysical evidence for deep subduction of continental crust beneath the Pamir* (Vol. 281). Boulder, CO: Geological Society of America.

Chen, B., Chen, C., Kaban, M. K., Du, J. S., Liang, Q., & Thomas, M. (2013). Variations of the effective elastic thickness over China and surroundings and their relation to the lithosphere dynamics. *Earth and Planetary Science Letters*, *363*, 61–72. https://doi.org/10.1016/j.epsl.2012.12.022

Chen, B., Liu, J. X., Chen, C., Du, J. S., & Sun, Y. (2015). Elastic thickness of the Himalayan-Tibetan orogen estimated from the fan wavelet coherence method, and its implications for lithospheric structure. *Earth and Planetary Science Letters*, *409*, 1–14. https://doi.org/10.1016/j.epsl.2014.10.039

Chen, W., & Tenzer, R. (2017). Moho modeling in spatial domain: A case study under Tibet. *Advances in Space Research*, *59*(12), 2855–2869. https://doi.org/10.1016/j.asr.2017.03.015

Deng, Y., Levandowski, W., & Kusky, T. (2017). Lithospheric density structure beneath the Tarim basin and surroundings, northwestern China, from the joint inversion of gravity and topography. *Earth and Planetary Science Letters*, *460*, 244–254. https://doi.org/10.1016/j.epsl.2016.10.051

Dewey, J. F., Shackleton, R. M., Chengfa, C., & Yiyin, S. (1988). The tectonic evolution of the Tibetan Plateau. *Philosophical Transactions of the Royal Society of London. Series A, Mathematical and Physical Sciences*, *327*(1594), 379–413. https://doi.org/10.1098/rsta.1988.0135

Feng, R., Yan, H.-F., & Zhang, R.-S. (1986). The rapid inversion of 3-D potential-field and program design. *Acta Geologica Sinica*, *60*(4), 83–96. https://doi.org/10.1111/j.1755-6724.1986.mp60004008.x

Förste, C., Bruinsma, S., Abrikosov, O., Flechtner, F., Marty, J.-C., Lemoine, J.-M., et al. (2014). EIGEN-6C4-The latest combined global gravity field model including GOCE data up to degree and order 1949 of GFZ Potsdam and GRGS Toulouse. Paper presented at the EGU general assembly conference abstracts.

Gao, R., Chen, C., Lu, Z. W., Brown, L. D., Xiong, X. S., Li, W. H., & Deng, G. (2013). New constraints on crustal structure and Moho topography in Central Tibet revealed by SinoProbe deep seismic reflection profiling. *Tectonophysics*, *606*, 160–170. https://doi.org/10.1016/j.tecto.2013.08.006

Gómez-Ortiz, D., & Agarwal, B. N. (2005). 3DINVER. M: A MATLAB program to invert the gravity anomaly over a 3D horizontal density interface by Parker–Oldenburg's algorithm. *Computers & Geosciences*, *31*(4), 513–520. https://doi.org/10.1016/j.cageo.2004.11.004

Hatzfeld, D., & Molnar, P. (2010). Comparisons of the kinematics and deep structures of the Zagros and Himalaya and of the Iranian and Tibetan Plateaus and geodynamic implications. *Reviews of Geophysics*, *48*, RG2005. https://doi.org/10.1029/2009RG000304

Kaban, M. K., El Khrepy, S., Al-Arifi, N., Tesauro, M., & Stolk, W. (2016). Three-dimensional density model of the upper mantle in the Middle East: Interaction of diverse tectonic processes. *Journal Of Geophysical Research: Solid Earth*, *121*, 5349–5364. https://doi.org/10.1002/2015JB012755

Kaban, M. K., Mooney, W. D., & Petrunin, A. G. (2015). Cratonic root beneath North America shifted by basal drag from the convecting mantle. *Nature Geoscience*, *8*(10), 797–800. https://doi.org/10.1038/ngeo2525

Kaban, M. K., Stolk, W., Tesauro, M., El Khrepy, S., Al-Arifi, N., Beekman, F., & Cloetingh, S. A. P. L. (2016). 3D density model of the upper mantle of Asia based on inversion of gravity and seismic tomography data. *Geochemistry, Geophysics, Geosystems*, *17*, 4457–4477. https://doi.org/10.1002/2016GC006458

Kaban, M. K., Tesauro, M., Mooney, W. D., & Cloetingh, S. A. (2014). Density, temperature, and composition of the North American lithosphere—New insights from a joint analysis of seismic, gravity, and mineral physics data: 1. Density structure of the crust and upper mantle. *Geochemistry, Geophysics, Geosystems*, *15*, 4781–4807. https://doi.org/10.1002/2014GC005483

Kind, R., Yuan, X., Saul, J., Nelson, D., Sobolev, S. V., Mechie, J., et al. (2002). Seismic images of crust and upper mantle beneath Tibet: Evidence for Eurasian plate subduction. *Science*, *298*(5596), 1219–1221. https://doi.org/10.1126/science.1078115

Koulakov, I., Maksotova, G., Mukhopadhyay, S., Raoof, J., Kayal, J. R., Jakovlev, A., & Vasilevsky, A. (2015). Variations of the crustal thickness in Nepal Himalayas based on tomographic inversion of regional earthquake data. *Solid Earth*, *6*(1), 207–216. https://doi.org/10.5194/se-6-207-2015

Kumar, P., Yuan, X., Kind, R., & Ni, J. (2006). Imaging the colliding Indian and Asian lithospheric plates beneath Tibet. *Journal of Geophysical Research*, *111*, B06308. https://doi.org/10.1029/2005JB003930

Laske, G., Masters, G., Ma, Z., & Pasyanos, M. (2013). Update on CRUST1. 0—A 1-degree global model of Earth's crust. Paper presented at the Geophys. Res. Abstr. http://igppweb.ucsd.edu/~gabi/crust1.html

Lawrence, I., & Lin, K. (1989). A concordance correlation coefficient to evaluate reproducibility. *Biometrics*, 255–268. https://www.jstor.org/stable/2532051

Li, X., & Chouteau, M. (1998). Three-dimensional gravity modeling in all space. *Surveys in Geophysics*, *19*(4), 339–368. https://doi.org/10.1023/A:1006554408567

Li, Y. H., Gao, M. T., & Wu, Q. J. (2014). Crustal thickness map of the Chinese mainland from teleseismic receiver functions. *Tectonophysics*, *611*, 51–60. https://doi.org/10.1016/j.tecto.2013.11.019

Lou, H., Wang, C., Lü, Z., Yao, Z., Dai, S., & You, H. (2009). Deep tectonic setting of the 2008 Wenchuan M S 8.0 earthquake in southwestern China. *Science in China Series D: Earth Sciences*, *52*(2), 166–179. https://doi.org/10.1007/s11430-009-0009-z

Lu, Z. W., Gao, R., Li, Q. S., He, R. Z., Kuang, C. Y., Hou, H. S., et al. (2009). Test of deep eismic reflection profiling across central uplift of Qiangtang Terrane in Tibetan Plateau. *Journal of Earth Science*, *20*(2), 438–447. https://doi.org/10.1007/s12583-009-0036-x

Mechie, J., & Kind, R. (2013). A model of the crust and mantle structure down to 700 km depth beneath the Lhasa to Golmud transect across the Tibetan plateau as derived from seismological data. *Tectonophysics*, *606*, 187–197. https://doi.org/10.1016/j.tecto.2013.04.030

Mechie, J., Kind, R., & Saul, J. (2011). The seismological structure of the Tibetan Plateau crust and mantle down to 700 km depth. *Geological Society, London, Special Publications*, *353*(1), 109–125. https://doi.org/10.1144/SP353.7

Nábělek, J., Hetenyi, G., Vergne, J., Sapkota, S., Kafle, B., Jiang, M., et al. (2009). Underplating in the Himalaya-Tibet Collision Zone Revealed by the Hi-CLIMB Experiment. *Science*, *325*(5946), 1371–1374. https://doi.org/10.1126/science.1167719

Nagendra, R., Prasad, P. V. S., & Bhimasankaram, V. L. S. (1996). Forward and inverse computer modeling of a gravity field resulting from a density interface using Parker-Oldenberg method. *Computers & Geosciences*, *22*(3), 227–237. https://doi.org/10.1016/0098-3004(95)00075-5

Obrebski, M., Allen, R. M., Zhang, F. X., Pan, J. T., Wu, Q. J., & Hung, S. H. (2012). Shear wave tomography of China using joint inversion of body and surface wave constraints. *Journal of Geophysical Research*, *117*, B01311. https://doi.org/10.1029/2011JB008349

O'Donnell, J. P., & Nyblade, A. A. (2014). Antarctica's hypsometry and crustal thickness: Implications for the origin of anomalous topography in East Antarctica. *Earth and Planetary Science Letters*, *388*, 143–155. https://doi.org/10.1016/j.epsl.2013.11.051

Oldenburg, D. W. (1974). The inversion and interpretation of gravity anomalies. *Geophysics*, *39*(4), 526–536. https://doi.org/10.1190/1.1440444

Parker, R. (1973). The rapid calculation of potential anomalies. *Geophysical Journal International*, *31*(4), 447–455. https://doi.org/10.1111/j.1365-246X.1973.tb06513.x

Prasanna, H. M. I., Chen, W., & Iz, H. B. (2013). High resolution local Moho determination using gravity inversion: A case study in Sri Lanka. *Journal of Asian Earth Sciences*, *74*, 62–70. https://doi.org/10.1016/j.jseaes.2013.06.005

Royden, L. H., Burchfiel, B. C., King, R. W., Wang, E., Chen, Z., Shen, F., & Liu, Y. (1997). Surface deformation and lower crustal flow in eastern Tibet. *Science*, *276*(5313), 788–790. https://doi.org/10.1126/science.276.5313.788

Royden, L. H., Burchfiel, B. C., & van der Hilst, R. D. (2008). The geological evolution of the Tibetan plateau. *Science*, *321*(5892), 1054–1058. https://doi.org/10.1126/science.1155371

Schaeffer, A. J., & Lebedev, S. (2013). Global shear speed structure of the upper mantle and transition zone. *Geophysical Journal International*, *194*(1), 417–449. https://doi.org/10.1093/gji/ggt095

Schneider, F. M., Yuan, X., Schurr, B., Mechie, J., Sippl, C., Haberland, C., et al. (2013). Seismic imaging of subducting continental lower crust beneath the Pamir. *Earth and Planetary Science Letters*, *375*, 101–112. https://doi.org/10.1016/j.epsl.2013.05.015

Shi, D. N., Zhao, W. J., Klemperer, S. L., Wu, Z. H., Mechie, J., Shi, J. Y., et al. (2016). West-east transition from underplating to steep subduction in the India-Tibet collision zone revealed by receiver-function profiles. *Earth and Planetary Science Letters*, *452*, 171–177. https://doi.org/10.1016/j.epsl.2016.07.051

Shin, Y. H., Shum, C. K., Braitenberg, C., Lee, S. M., Na, S. H., Choi, K. S., et al. (2015). Moho topography, ranges and folds of Tibet by analysis of global gravity models and GOCE data. *Scientific Reports*, *5*, 11681. https://doi.org/10.1038/srep11681

Shin, Y. H., Shum, C. K., Braitenberg, C., Lee, S. M., Xu, H. Z., Choi, K. S., et al. (2009). Three-dimensional fold structure of the Tibetan Moho from GRACE gravity data. *Geophysical Research Letters*, *36*, L01302. https://doi.org/10.1029/2008GL036068

Shin, Y. H., Xu, H., Braitenberg, C., Fang, J., & Wang, Y. (2007). Moho undulations beneath Tibet from GRACE-integrated gravity data. *Geophysical Journal International*, *170*(3), 971–985. https://doi.org/10.1111/j.1365-246X.2007.03457.x

Singh, A., Kumar, M. R., Mohanty, D. D., Singh, C., Biswas, R., & Srinagesh, D. (2017). Crustal structure beneath India and Tibet: New constraints from inversion of receiver functions. *Journal Of Geophysical Research: Solid Earth*, *122*, 7839–7859. https://doi.org/10.1002/2017JB013946

Sjoberg, L. E. (2009). Solving Vening Meinesz-Moritz inverse problem in isostasy. *Geophysical Journal International*, *179*(3), 1527–1536. https://doi.org/10.1111/j.1365-246X.2009.04397.x

Sjoberg, L. E. (2013). On the isostatic gravity anomaly and disturbance and their applications to Vening Meinesz-Moritz gravimetric inverse problem. *Geophysical Journal International*, *193*(3), 1277–1282. https://doi.org/10.1093/gji/ggt008

Steffen, R., Steffen, H., & Jentzsch, G. (2011). A three-dimensional Moho depth model for the Tien Shan from EGM2008 gravity data. *Tectonics*, *30*, TC5019. https://doi.org/10.1029/2011TC002886

Stolk, W., Kaban, M., Beekman, F., Tesauro, M., Mooney, W. D., & Cloetingh, S. (2013). High resolution regional crustal models from irregularly distributed data: Application to Asia and adjacent areas. *Tectonophysics*, *602*, 55–68. https://doi.org/10.1016/j.tecto.2013.01.022

Sun, Y., Niu, F. L., Liu, H. F., Chen, Y. L., & Liu, J. X. (2012). Crustal structure and deformation of the SE Tibetan plateau revealed by receiver function data. *Earth and Planetary Science Letters*, *349-350*, 186–197. https://doi.org/10.1016/j.epsl.2012.07.007

Szwillus, W., Afonso, J. C., Ebbing, J., & Mooney, W. D. (2019). Global crustal thickness and velocity structure from geostatistical analysis of seismic data. *Journal Of Geophysical Research: Solid Earth*, *124*, 1626–1652. https://doi.org/10.1029/2018JB016593

Tapponnier, P., Peltzer, G., Le Dain, A., Armijo, R., & Cobbold, P. (1982). Propagating extrusion tectonics in Asia: New insights from simple experiments with plasticine. *Geology*, *10*(12), 611–616. https://doi.org/10.1130/0091-7613(1982)10<611:PETIAN>2.0.CO;2

Tapponnier, P., Zhiqin, X., Roger, F., Meyer, B., Arnaud, N., Wittlinger, G., & Jingsui, Y. (2001). Oblique stepwise rise and growth of the Tibet Plateau. *Science*, *294*(5547), 1671–1677. https://doi.org/10.1126/science.105978

Teng, J. W., Deng, Y. F., Badal, J., & Zhang, Y. Q. (2014). Moho depth, seismicity and seismogenic structure in China mainland. *Tectonophysics*, *627*, 108–121. https://doi.org/10.1016/j.tecto.2013.11.008

Teng, J. W., Zhang, Z. J., Zhang, X. K., Wang, C. Y., Gao, R., Yang, B. J., et al. (2013). Investigation of the Moho discontinuity beneath the Chinese mainland using deep seismic sounding profiles. *Tectonophysics*, *609*, 202–216. https://doi.org/10.1016/j.tecto.2012.11.024

Tenzer, R., Bagherbandi, M., Hwang, C., & Tsui-Yu Chang, E. (2013). Moho interface modeling beneath the Himalayas, Tibet and Central Siberia using GOCO02S and DTM2006. *Terrestrial, Atmospheric and Oceanic Sciences*, *24*(4-1), 581–590. https://doi.org/10.3319/TAO.2012.11.01.02(TibXS)

Tenzer, R., & Chen, W. (2019). Mantle and sub-lithosphere mantle gravity maps from the LITHO1.0 global lithospheric model. *Earth-Science Reviews*, *194*, 38–56. https://doi.org/10.1016/j.earscirev.2019.05.001

Tenzer, R., Chen, W., & Jin, S. (2015). Effect of upper mantle density structure on Moho geometry. *Pure and Applied Geophysics*, *172*(6), 1563–1583. https://doi.org/10.1007/s00024-014-0960-2

Tenzer, R., Chen, W., Tsoulis, D., Bagherbandi, M., Sjöberg, L. E., Novák, P., & Jin, S. (2015). Analysis of the refined CRUST1. 0 crustal model and its gravity field. *Surveys in Geophysics*, *36*(1), 139–165. http://doi.org/10.1007/s10712-014-9299-6

Tenzer, R., Hamayun, K., & Vajda, P. (2009). Global maps of the CRUST 2.0 crustal components stripped gravity disturbances. *Journal of Geophysical Research*, *114*, B05408. https://doi.org/10.1029/2008JB006016

Tian, X. B., Liu, Z., Si, S. K., & Zhang, Z. J. (2014). The crustal thickness of NE Tibet and its implication for crustal shortening. *Tectonophysics*, *634*, 198–207. https://doi.org/10.1016/j.tecto.2014.07.001

Tilmann, F., Ni, J., & INDEPTH III Seismic Team (2003). Seismic imaging of the downwelling Indian lithosphere beneath central Tibet. *Science*, *300*(5624), 1424–1427. https://doi.org/10.1126/science.1082777

Uieda, L., & Barbosa, V. C. F. (2017). Fast nonlinear gravity inversion in spherical coordinates with application to the South American Moho. *Geophysical Journal International*, *208*(1), 162–176. https://doi.org/10.1093/gji/ggw390

van der Meijde, M., Julia, J., & Assumpcao, M. (2013). Gravity derived Moho for South America. *Tectonophysics*, *609*, 456–467. https://doi.org/10.1016/j.tecto.2013.03.023

Wang, W. L., Wu, J. P., Fang, L. H., Lai, G. J., & Cai, Y. (2017). Sedimentary and crustal thicknesses and Poisson's ratios for the NE Tibetan Plateau and its adjacent regions based on dense seismic arrays. *Earth and Planetary Science Letters*, *462*, 76–85. https://doi.org/10.1016/j.epsl.2016.12.040

Willett, S. D., & Beaumont, C. (1994). Subduction of Asian lithospheric mantle beneath Tibet inferred from models of continental collision. *Nature*, *369*(6482), 642–645. https://doi.org/10.1038/369642a0

Wu, L. Y. (2016). Efficient modelling of gravity effects due to topographic masses using the Gauss-FFT method. *Geophysical Journal International*, *205*(1), 160–178. https://doi.org/10.1093/gji/ggw010

Wu, L. Y., & Tian, G. (2014). High-precision Fourier forward modeling of potential fields. *Geophysics*, *79*(5), G59–G68. https://doi.org/10.1190/geo2014-0039.1

Xia, J. H., & Sprowl, D. R. (1995). Moho depths in Kansas from gravity inversion assuming exponential density contrast. *Computers & Geosciences*, *21*(2), 237–244. https://doi.org/10.1016/0098-3004(94)00068-6

Xu, C., Liu, Z. W., Luo, Z. C., Wu, Y. H., & Wang, H. H. (2017). Moho topography of the Tibetan Plateau using multi-scale gravity analysis and its tectonic implications. *Journal of Asian Earth Sciences*, *138*, 378–386. https://doi.org/10.1016/j.jseaes.2017.02.028

Yin, A., & Harrison, T. M. (2000). Geologic evolution of the Himalayan-Tibetan orogen. *Annual Review of Earth and Planetary Sciences*, *28*(1), 211–280. https://doi.org/10.1146/annurev.earth.28.1.211

Zhang, C., Huang, D. N., Wu, G. C., Ma, G. Q., Yuan, Y., & Yu, P. (2015). Calculation of Moho Depth by Gravity Anomalies in Qinghai-Tibet Plateau Based on an Improved Iteration of Parker-Oldenburg Inversion. *Pure and Applied Geophysics*, *172*(10), 2657–2668. https://doi.org/10.1007/s00024-015-1039-4

Zhang, H. S., Teng, J. W., Tian, X. B., Zhang, Z. J., Gao, R., & Liu, J. Q. (2012). Lithospheric thickness and upper-mantle deformation beneath the NE Tibetan Plateau inferred from S receiver functions and SKS splitting measurements. *Geophysical Journal International*, *191*(3), 1285–1294. https://doi.org/10.1111/j.1365-246X.2012.05667.x

Zhang, Z. J., Deng, Y. F., Chen, L., Wu, J., Teng, J. W., & Panza, G. (2013). Seismic structure and rheology of the crust under mainland China. *Gondwana Research*, *23*(4), 1455–1483. https://doi.org/10.1016/j.gr.2012.07.010

Zhang, Z. J., & Klemperer, S. L. (2005). West-east variation in crustal thickness in northern Lhasa block, central Tibet, from deep seismic sounding data. *Journal of Geophysical Research*, *110*, B09403. https://doi.org/10.1029/2004JB003139

Zhang, Z. J., Wang, Y. H., Houseman, G. A., Xu, T., Wu, Z. B., Yuan, X. H., et al. (2014). The Moho beneath western Tibet: Shear zones and eclogitization in the lower crust. *Earth and Planetary Science Letters*, *408*, 370–377. https://doi.org/10.1016/j.epsl.2014.10.022

Zhao, G. D., Chen, B., Chen, L. W., Liu, J. X., & Ren, Z. Y. (2018). High-accuracy 3D Fourier forward modeling of gravity field based on the Gauss-FFT technique. *Journal of Applied Geophysics*, *150*, 294–303. https://doi.org/10.1016/j.jappgeo.2018.01.002

Zhao, G. D., Chen, B., Uieda, L., Liu, J., Kaban, M. K., Chen, L., & Guo, R. (2019). Efficient 3D large-scale forward-modeling and inversion of gravitational fields in spherical coordinates with application to lunar mascons. *Journal of Geophysical Research: Solid Earth*, *124*, 4157–4173. https://doi.org/10.1029/2019JB017691

Zhao, W. J., Kumar, P., Mechie, J., Kind, R., Meissner, R., Wu, Z. H., et al. (2011). Tibetan plate overriding the Asian plate in central and northern Tibet. *Nature Geoscience*, *4*(12), 870–873. https://doi.org/10.1038/ngeo1309